Electronic Supplementary Information

Large-Scale and Solvent-Free Synthesis of Magnetic Bamboo-Like Nitrogen-Doped Carbon Nanotubes with Nickel Active Sites for Photothermal-Driven CO_2 Fixation

Yingchun Guo,[a] Xinxin Wang,[b] Lei Feng,[b] Feng Liu,[c] Jinsheng Liang,[a] Xiaomei Wang*[b] and Xu Zhang*[b]*

[a] Key Laboratory of Special Functional Materials for Ecological Environment and Information, School of Materials Science and Engineering, Hebei University of Technology, Ministry of Education, Tianjin 300130, China

[b] Hebei Key Laboratory of Functional Polymers, School of Chemical Engineering and Technology, Hebei University of Technology, Tianjin 300130, China

[c] Institute of Materials Science and Devices, School of Materials Science and Engineering, Suzhou University of Science and Technology, Suzhou 215011, China

*Corresponding Author: E-mail: xmwang@hebut.edu.cn; xuzhang@hebut.edu.cn; liangjinsheng@hebut.edu.cn

Chemicals. All chemicals were purchased from commercial supplies and used without further purification. Nickel acetate ($Ni(CH_3COO)_2 \cdot 4H_2O$, 98%), zinc hydroxide ($Zn(OH)_2$, 98%), nickel nitrate hexahydrate ($Ni(NO_3)_2 \cdot 6H_2O$, 98%), zinc nitrate hexahydrate ($Zn(NO_3)_2 \cdot 6H_2O$, 98%) 2-methylimidazole (2-MeIM, 99%), and methanol (CH_3OH, 99%) were received from Tianjin Fuchen Chemical Corporation. Amines (>98%), phenylsilane ($PhSiH_3$, 98%), and *N, N*-Dimethylformamide (DMF, 98%) were received from Aladdin. Carbon dioxide and Ar gas were obtained from Tianjin Dongrun Gas Co., Ltd.

Characterizations. The morphology and structure were acquired by field-emission scanning electron microscopy with different accelerating voltages (SEM, FEI Nova NanoSEM450) and transmission electron microscopy (TEM, FEI Talos F200S, 200 kV). The aberration-corrected high-angle annular dark-field scanning transmission electron microscopy (AC-HAADF-STEM) measurements were taken on a Titan Themis Cubed G2 60-300, FEI. X-ray diffraction (XRD) patterns were investigated by a Bruker D8-Davinci equipped with Cu Kα radiation source. X-ray photoelectron spectroscopy (XPS) measurements were conducted on a Thermo Scientific ESCALab-250Xi spectrometer with monochromatic Al Kα radiation, and the binding energies were calibrated using the C 1s peak at 284.6 eV. Nitrogen adsorption-desorption isotherms were acquired on a surface area and porosity analyzer (Micromeritics ASAP 2020). The content of Ni atoms was investigated by an Optima 7300 DV inductively coupled plasma optical emission spectroscopy (ICP-OES). Fourier transform infrared (FT-IR) spectra were performed on a Bruker VECTOR-22 spectrometer. The ^{1}H-

nuclear magnetic resonance (NMR) spectra were analyzed and identified by a Bruker 400 spectrometer using $CDCl_3$ as a solvent and tetramethylsilane (TMS) as an internal standard. Electron paramagnetic resonance (EPR) spectra were collected by a Bruker EMXnano. Raman spectra were recorded on a Renishaw inVia Reflex UV Raman spectrometer with an excitation laser wavelength of $\lambda = 532$ nm. The obtained liquid solution after the reaction was identified by GC-MS. Magnetic hysteresis loops of the materials were measured at room temperature via a vibrating sample magnetometer (VSM, MPMS XL-7).

Computational details. All the calculations are performed in the framework of the density functional theory with the projector augmented plane-wave method, as implemented in the Vienna ab initio simulation package. The generalzied gradient approximation proposed by Perdew, Burke, and Ernzerhof is selected for the exchange-correlation potential. The long range van der Waals interaction is described by the DFT-D3 approach. The cut-off energy for plane wave is set to 550 eV. The energy criterion is set to 10^{-6} eV in iterative solution of the Kohn-Sham equation. A vacuum layer of 20 Å is added perpendicular to the sheet to avoid artificial interaction between periodic images. The Brillouin zone integration is performed using a 2x2x1 k-mesh. All the structures are relaxed until the residual forces on the atoms have declined to less than 0.01 eV/Å.

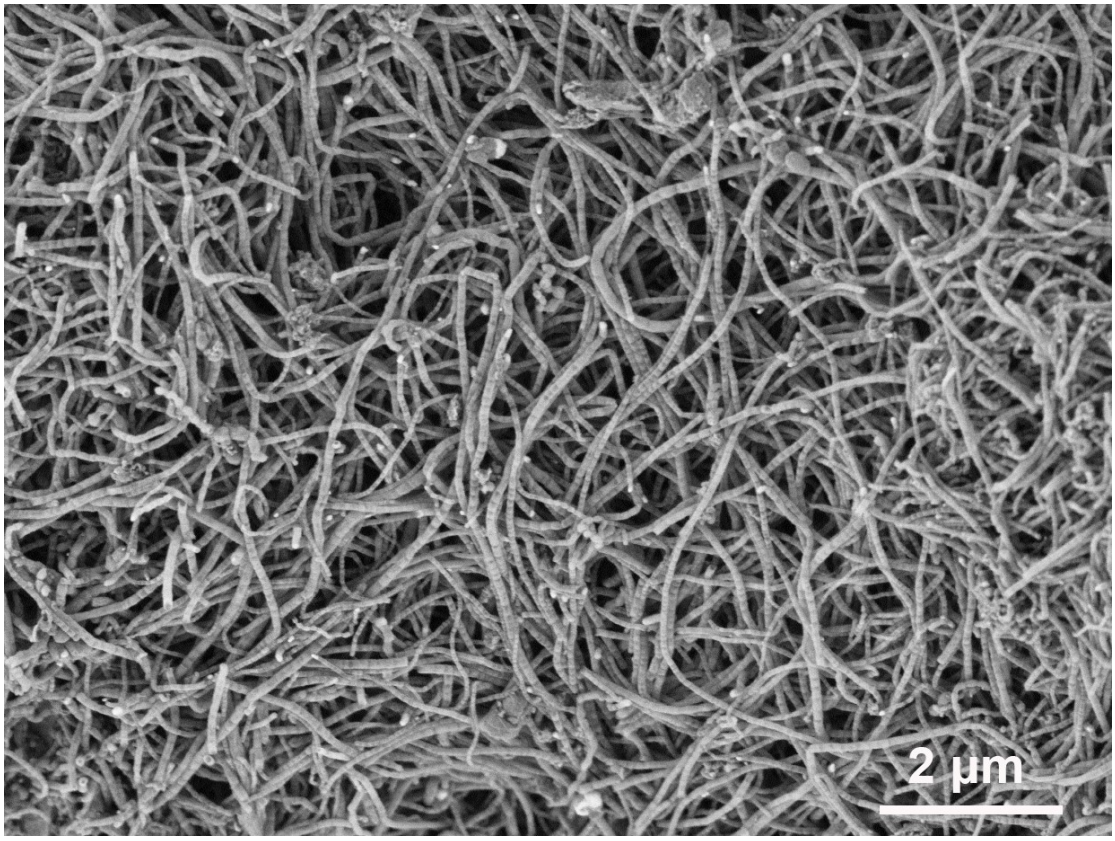

Figure S1. SEM image of Ni-SAs/NPs@BNCNTs (concentric backscattered retractable detector at 1 kV).

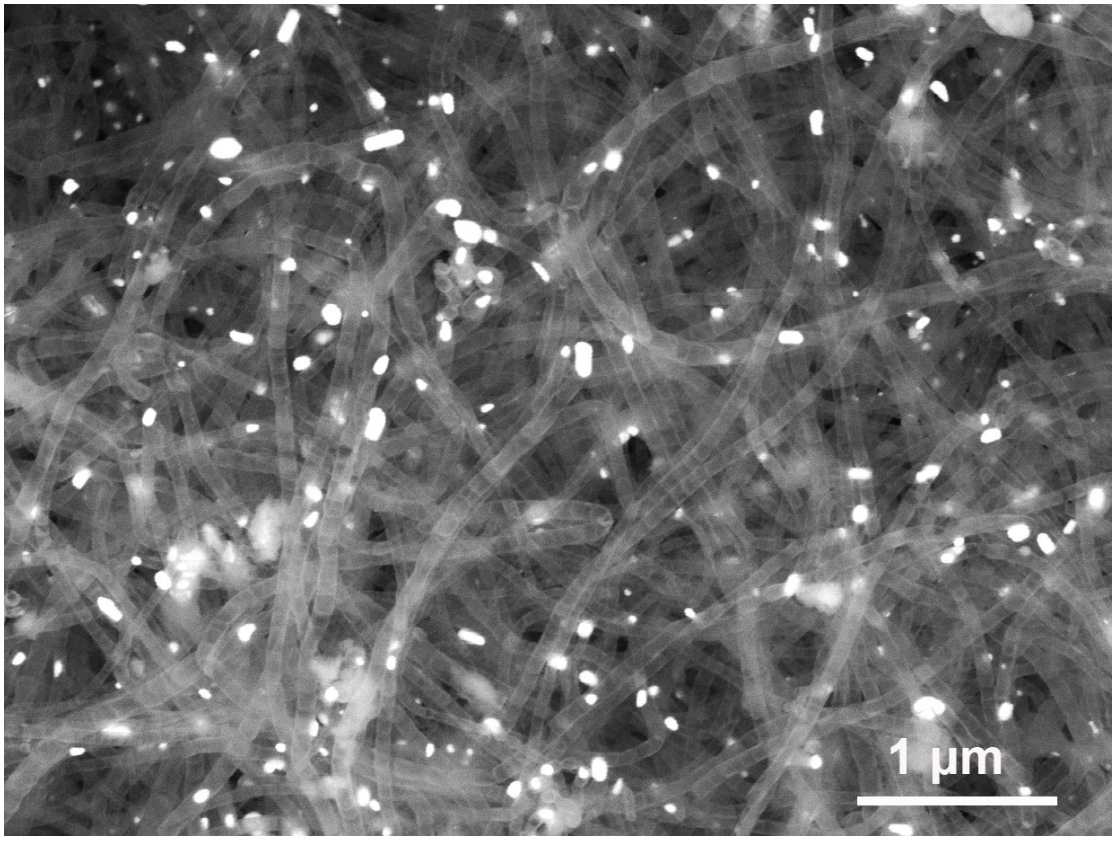

Figure S2. SEM image of Ni-SAs/NPs@BNCNTs (concentric backscattered retractable detector at 5 kV).

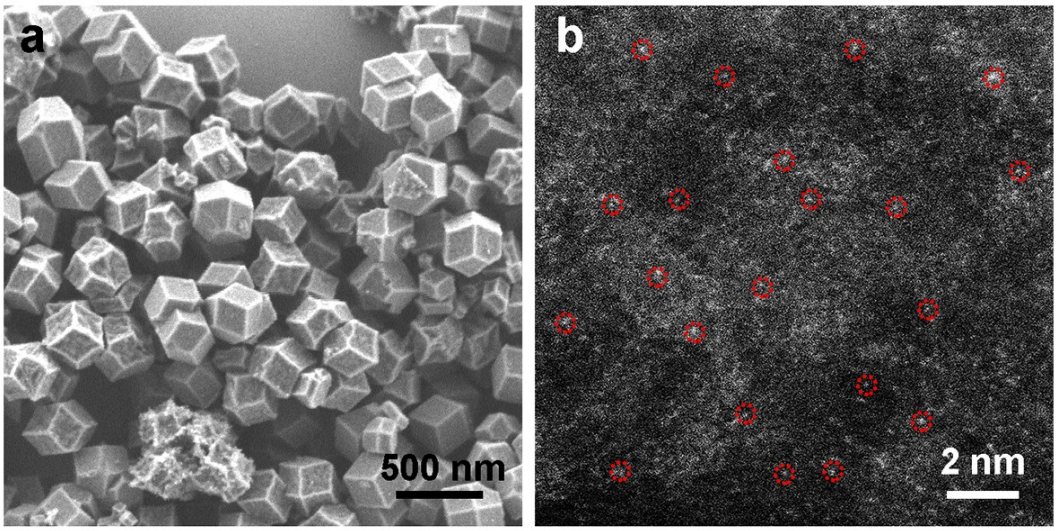

Figure S3. (a) SEM image and (b) aberration-corrected HAADF-STEM image of the Ni-SAs@NC.

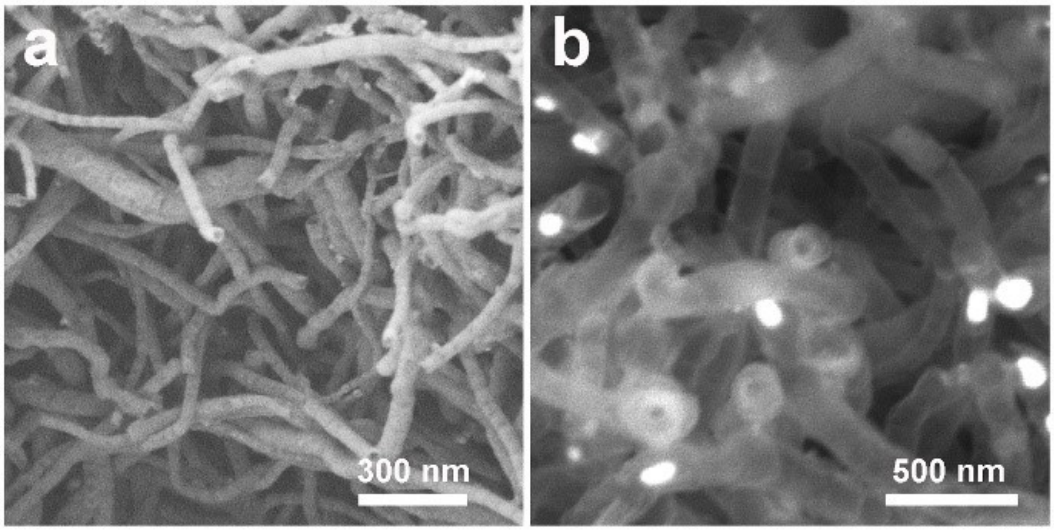

Figure S4. SEM images of the Ni-NPs@BNCNTs (a) concentric backscattered retractable detector at 1 kV and (b) at 5 kV.

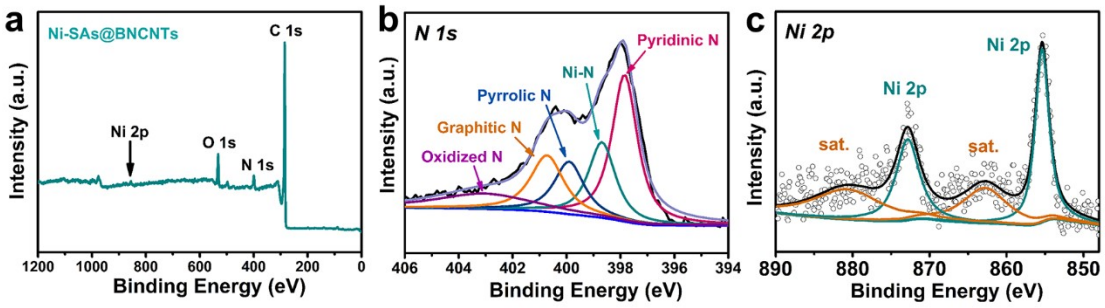

Figure S5. (a) Wide-survey XPS spectrum, (b) high-resolution N 1s XPS spectrum, and (c) high-resolution Ni 2p XPS spectrum of Ni-SAs@BNCNTs.

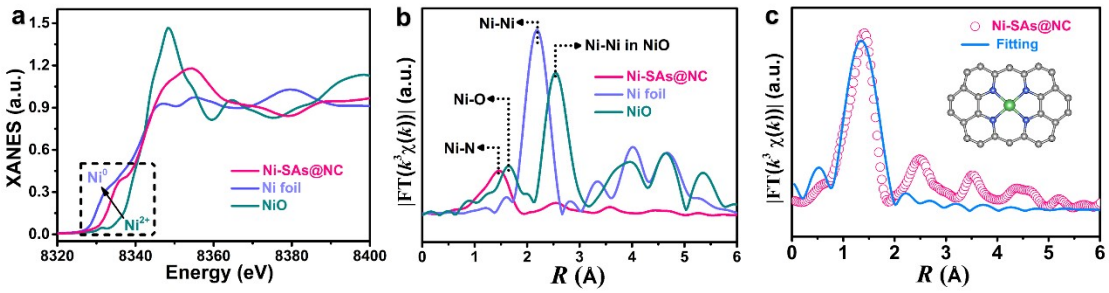

Figure S6. (a) Ni K-edge XANES and (b) Fourier transform (FT) Ni K-edge EXAFS spectra of Ni foil, NiO, and Ni-SAs@NC. (c) FT-EXAFS R-space fitting curve of Ni-SAs@NC. Inset: the model of Ni-SAs@NC.

To uncover the valence state and coordination environment of single-Ni atoms in Ni-SAs@NC, a synchrotron-based X-ray absorption test was performed. The X-ray absorption near-edge structure (XANES) spectra disclose that the energy absorption threshold values of Ni in Ni-SAs@NC lies between those of Ni foil and NiO, indicating the oxidation state of the single-Ni species between 0 and +2 (Figure 6a). Fourier transform-extended X-ray absorption fine structures (FT-EXAFS) of Ni-SAs@NC display Ni-N peaks at 1.4 Å without Ni-O (1.6 Å) or Ni-Ni bonds (2.2 Å), illustrating the single-atomic Ni dispersion (Figure 6b). Additionally, the EXAFS fittings result confirms that Ni–N_4 configuration is the dominant coordination mode of Ni atoms in Ni-SA@BNCNTs (Figure 6c).

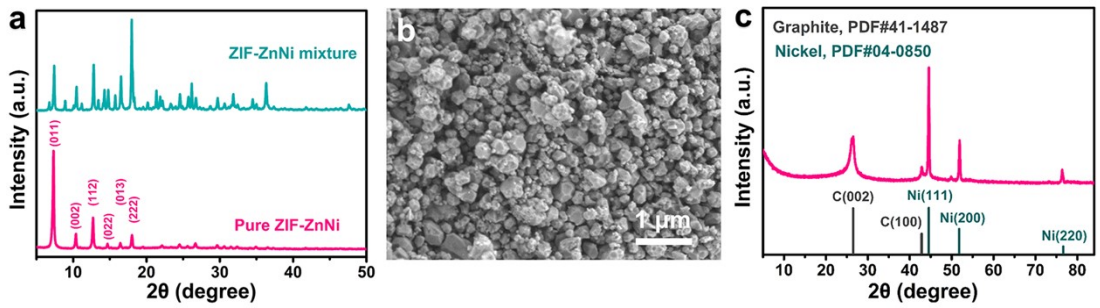

Figure S7. (a) XRD patterns of ZIF-ZnNi mixture and pure ZIF-ZnNi. (b) SEM image of the pure ZIF-ZnNi. (c) XRD pattern of Ni-SAs/NPs@BNCNTs.

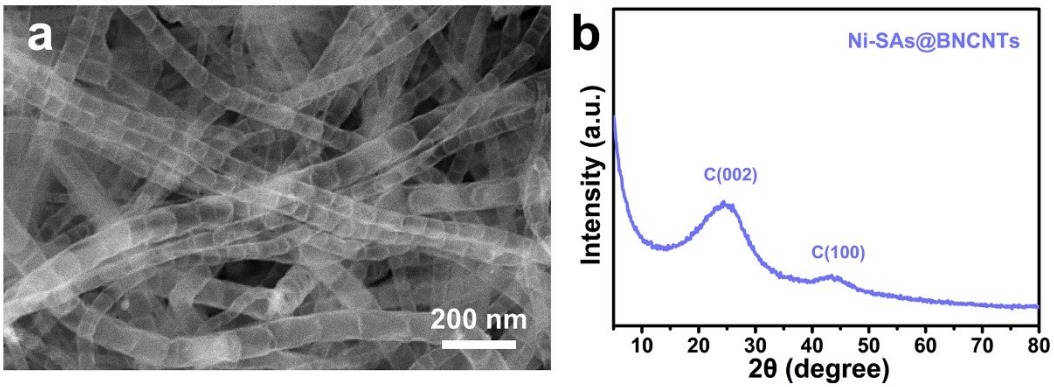

Figure S8. (a) SEM images of Ni-SAs@BNCNTs. (b) XRD pattern of the Ni-SAs@BNCNTs.

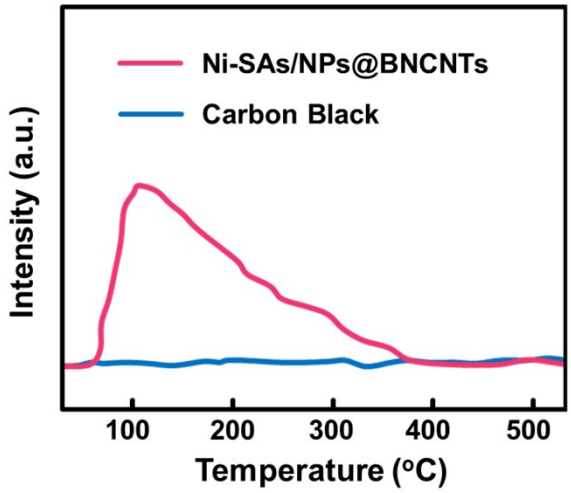

Figure S9. CO_2-TPD profiles of Ni-SAs/NPs@BNCNTs and carbon black.

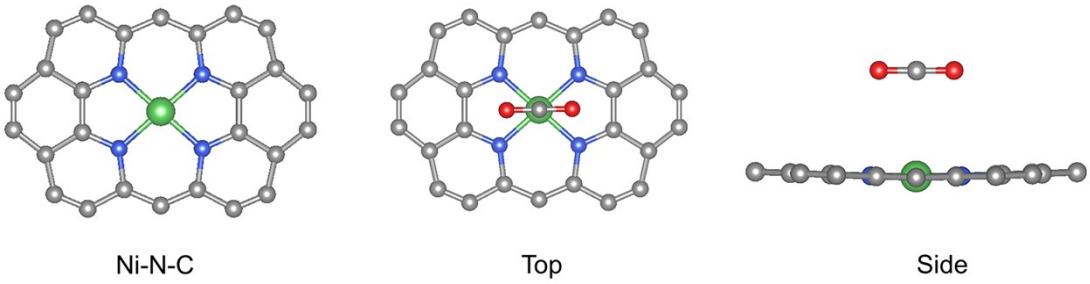

Figure S10. CO_2 adsorption model on Ni-N-C.

Table S1. The effect of photogenerated electrons on the adsorption energy of CO_2.

Adsorption Energy Data	Ni-N-C	Ni-N-C and e^-
E_b	0.224 eV	-0.072 eV
Ni-C_{CO2} (distance)	3.319 Å	3.285 Å

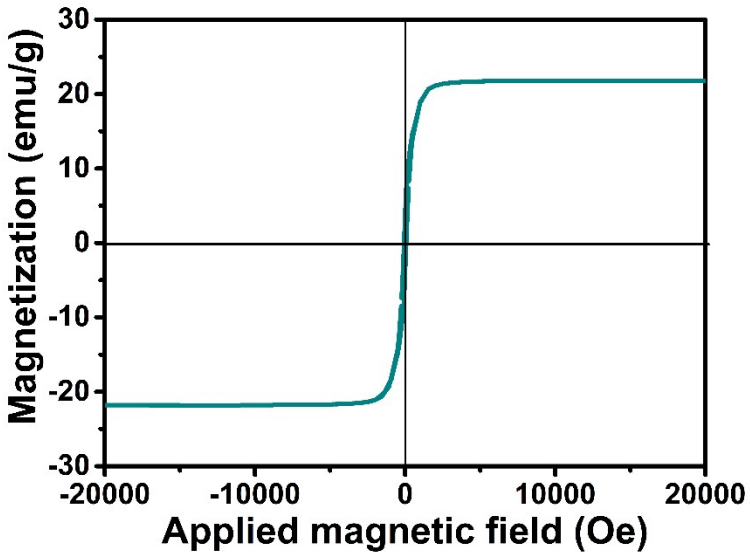

Figure S11. The magnetic hysteresis loop of Ni-NPs/SAs@BNCNTs.

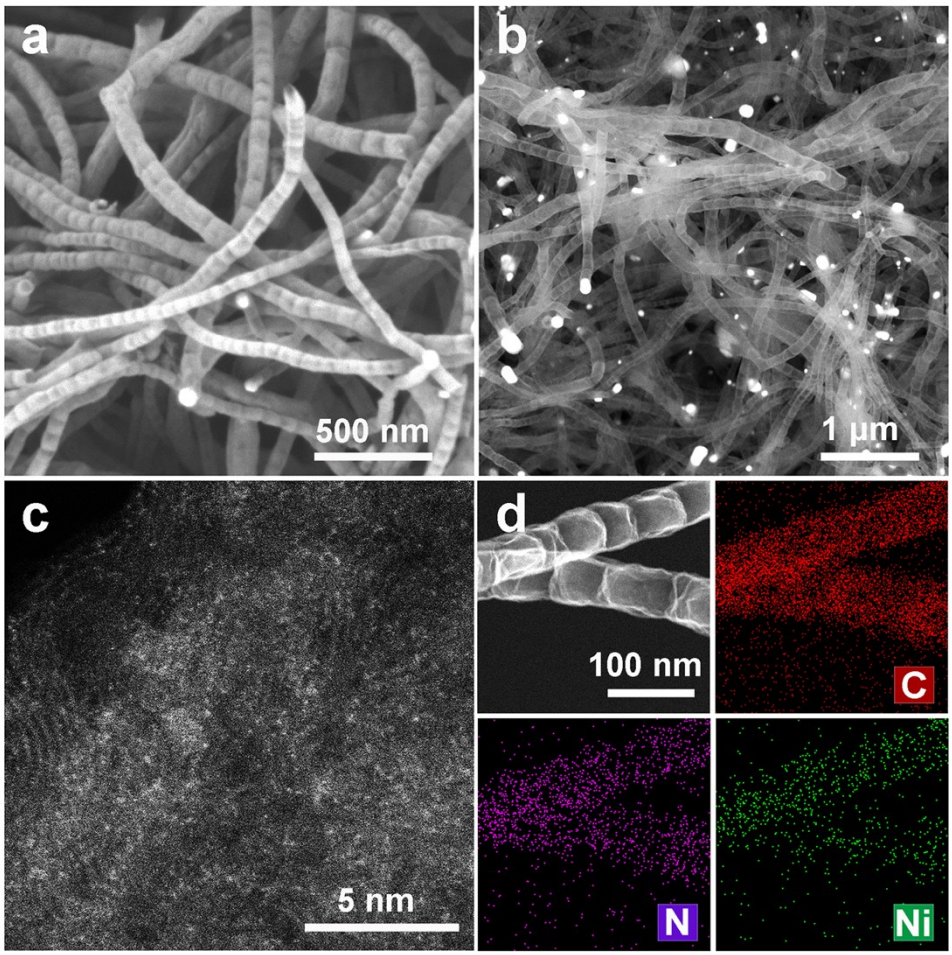

Figure S12. (a) SEM image (at 1 kV), (b) SEM image (at 5 kV), (c) Aberration-corrected HAADF-STEM image, and (d) HAADF-STEM image and corresponding element mappings of Ni-SAs/NPs@BNCNTs after using for 10 times.

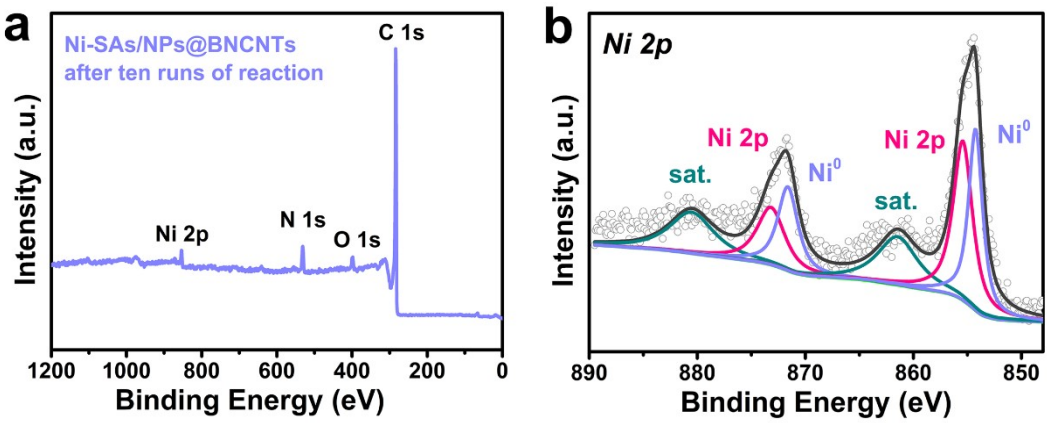

Figure S13. XPS spectra of Ni-SAs/NPs@BNCNTs after using for 10 times (a) survey scan and (b) Ni 2p.

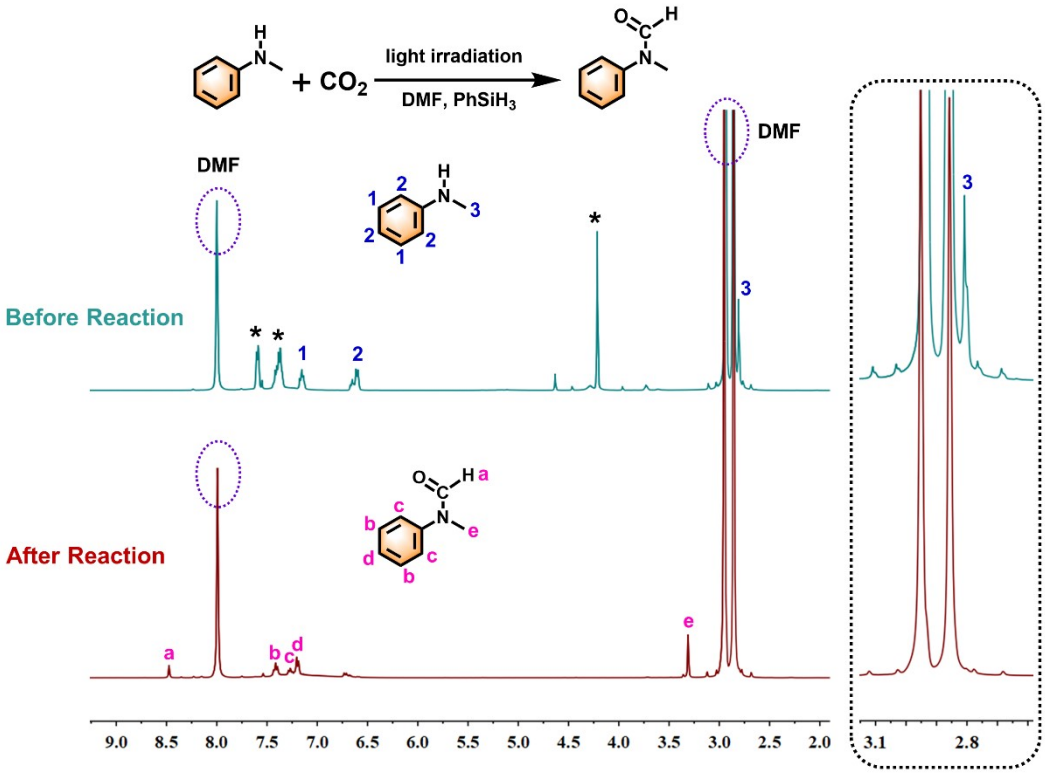

Figure S14. Crude ^{1}H-NMR spectra of *N*-formylation of *N*-methylaniline with CO_2 and $PhSiH_3$ by using Ni-SAs/NPs@BNCNTs. Signals with asterisk are related to $PhSiH_3$.

Product (*N*-methylformanilide). ^{1}H-NMR ($CDCl_3$, 400 MHz) δ 8.48 (s, 1H), δ 7.42 (t, J = 7.8 Hz, 2H), 7.28 (t, J = 7.4 Hz, 1H), 7.18 (d, J = 7.6 Hz, 2H), δ 3.33 (s, 3H).

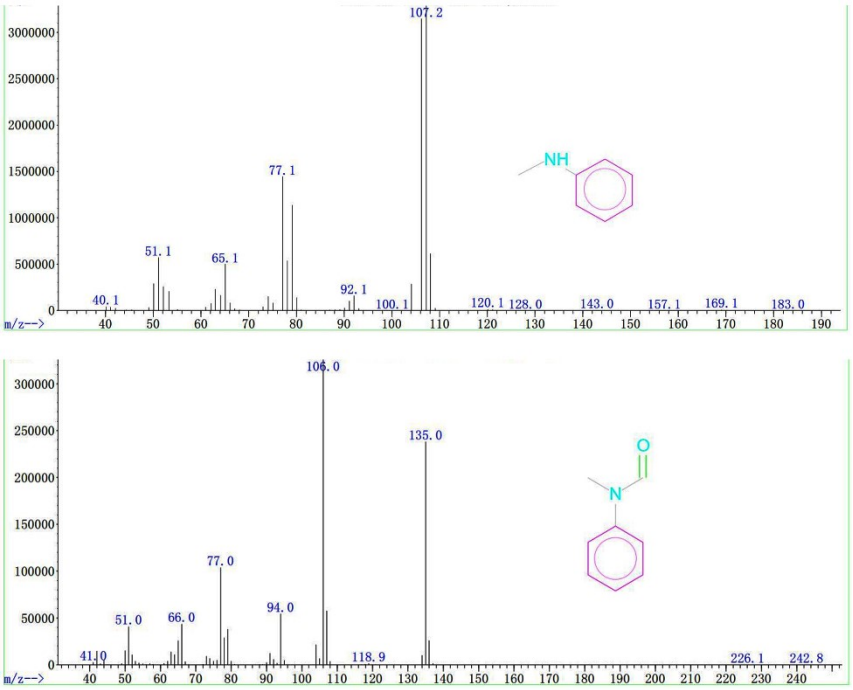

Figure S15. The mass spectra of *N*-methylaniline and *N*-methylformanilide.

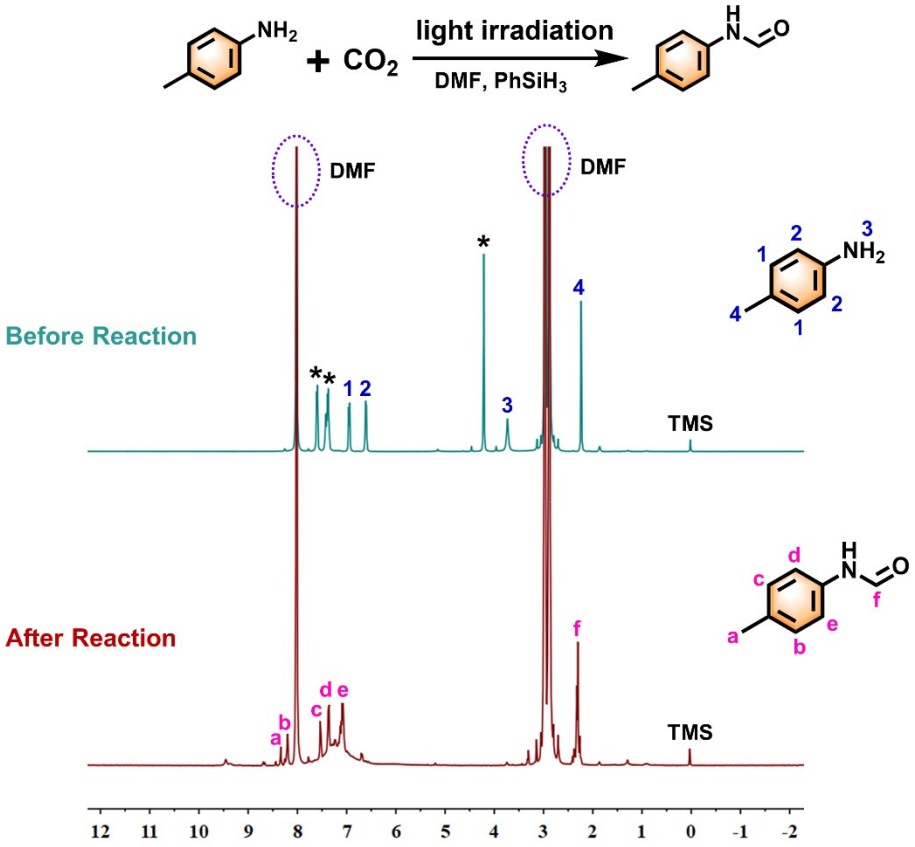

Figure S16. Crude ^{1}H-NMR spectra of *N*-formylation of *p*-toluidine with CO_2 and $PhSiH_3$ by using Ni-SAs/NPs@BNCNTs. Signals with asterisk are related to $PhSiH_3$.

Product (*N*-*p*-tolylformamide). ^{1}H-NMR ($CDCl_3$, 400 MHz) 8.42, 8.15 (d, J = 11.35 Hz, and br, total 1H), 7.42 (d, J = 8.72, 1H), 7.15 (t, J = 8.54, 2H), 6.97 (d, J = 8.01, 1H), 2.32 (d, J = 6.47, 3H).

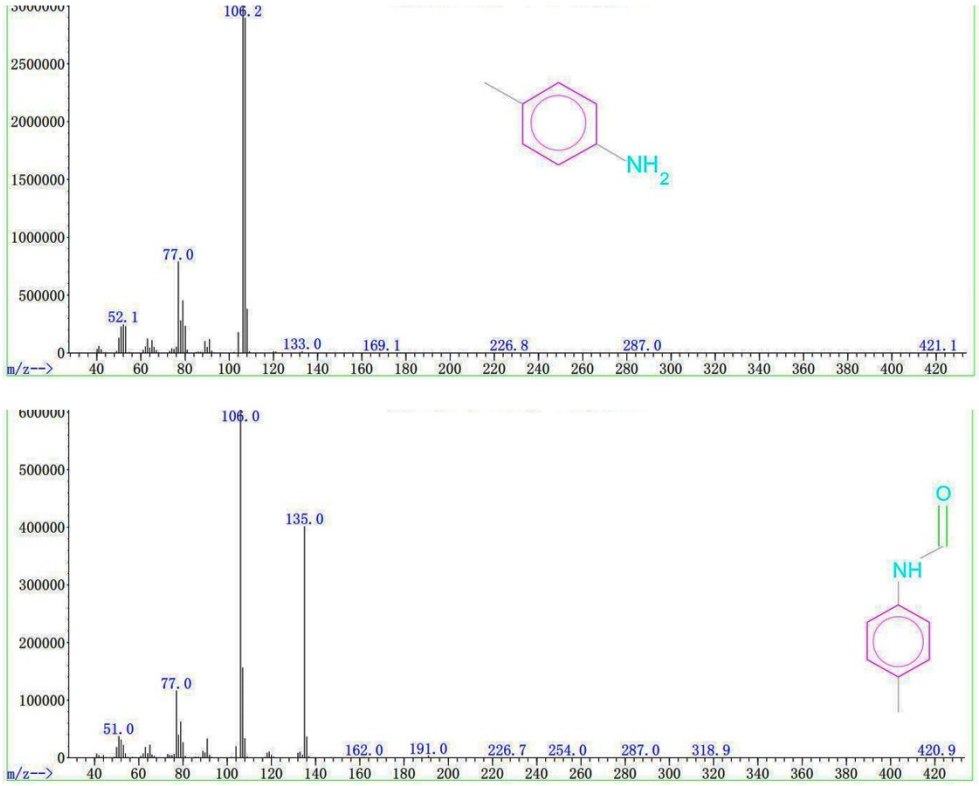

Figure S17. The mass spectra of *p*-toluidine and *N*-*p*-tolylformamide.

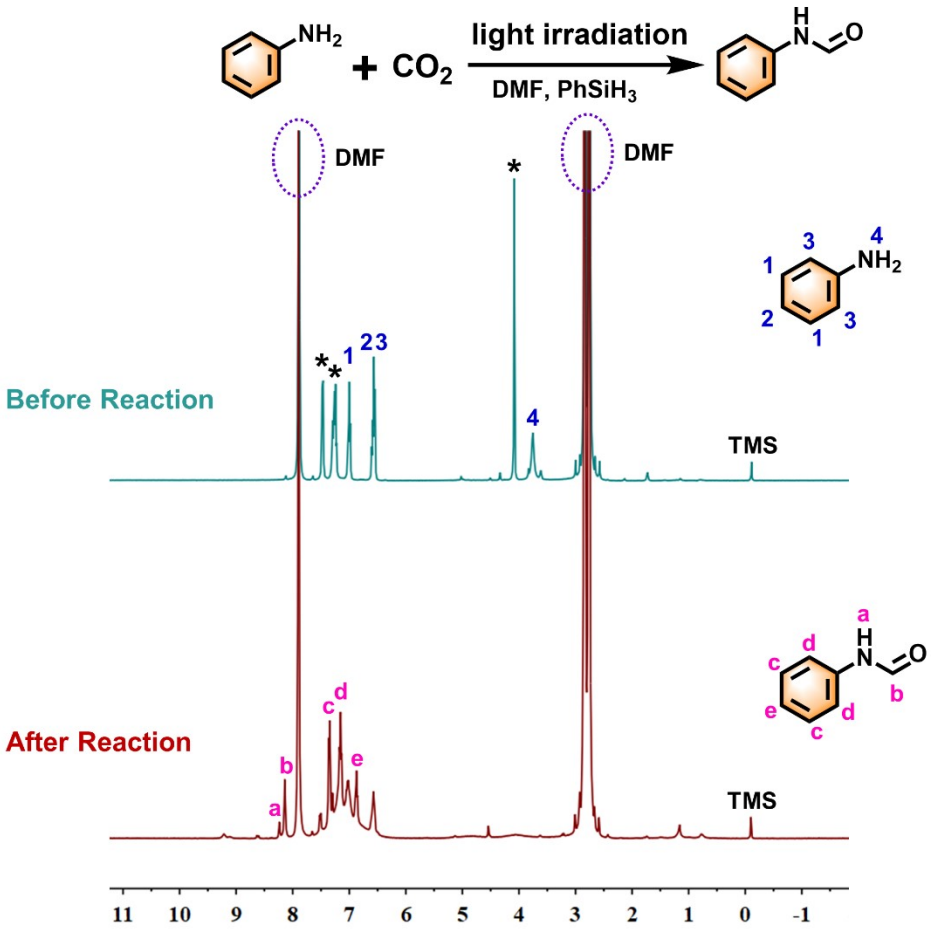

Figure S18. Crude ^{1}H-NMR spectra of *N*-formylation of aniline with CO_2 and $PhSiH_3$ by using Ni-SAs/NPs@BNCNTs. Signals with asterisk are related to $PhSiH_3$.

Product (*N*-phenylformamide). ^{1}H-NMR ($CDCl_3$, 400 MHz)□ δ = 8.68 (s, 1H), 8.36 (s, 1H), 7.60-7.48 (m, 1H), 7.43-7.28 (m, 2H), 7.24-7.05 (m, 2H).

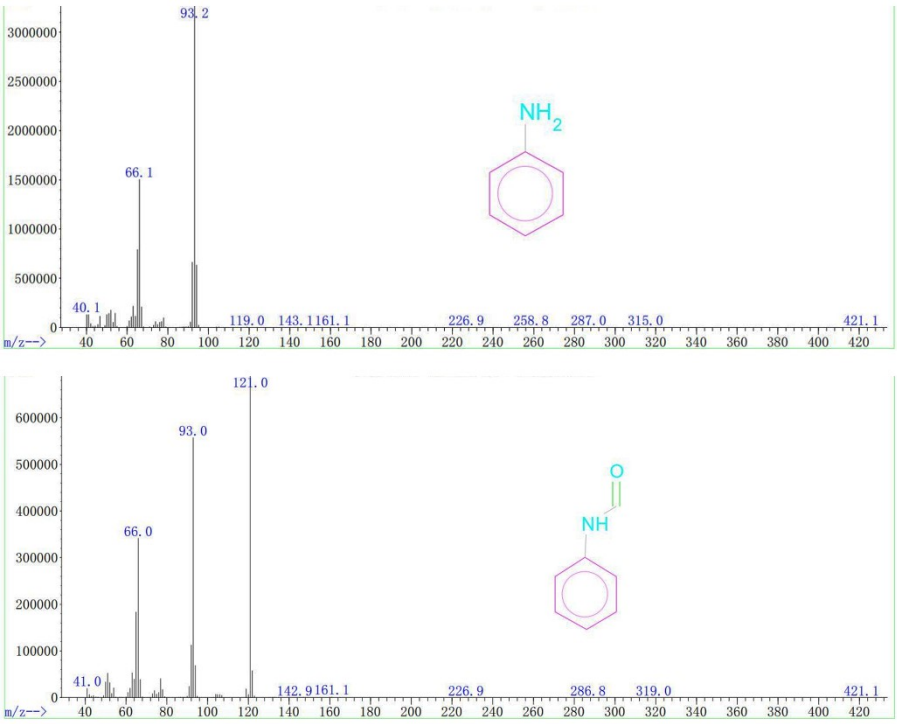

Figure S19. The mass spectra of aniline and *N*-phenylformamide.

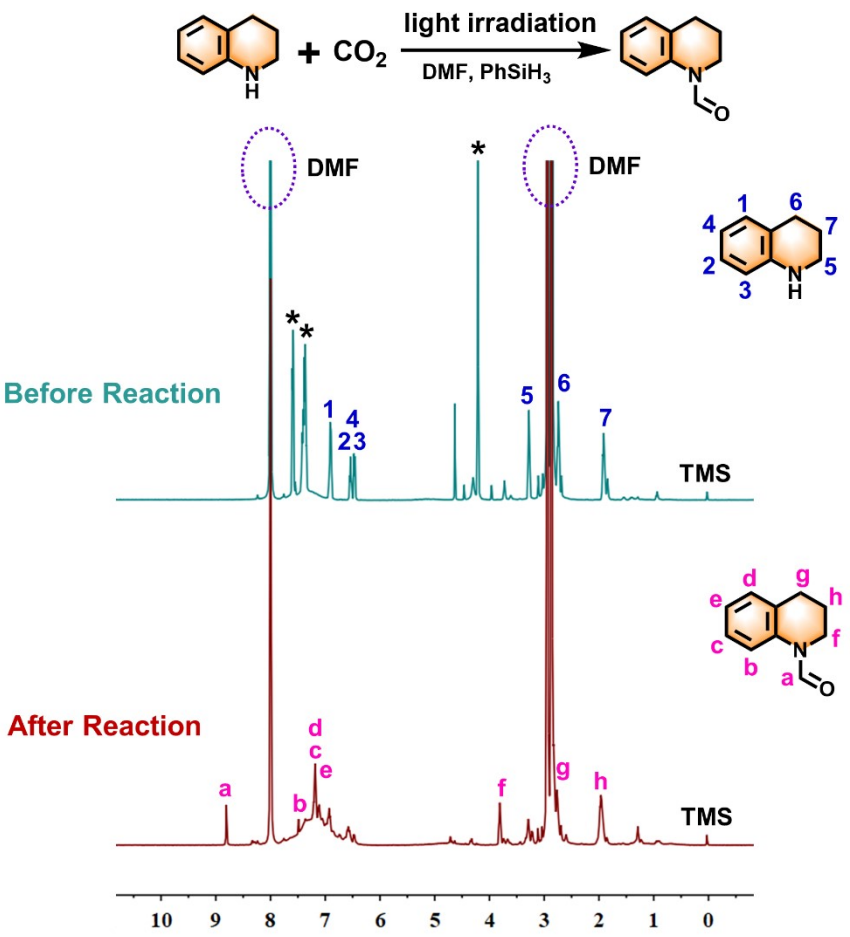

Figure S20. Crude ^{1}H-NMR spectra of *N*-formylation of aniline with CO_2 and $PhSiH_3$ by using Ni-SAs/NPs@BNCNTs. Signals with asterisk are related to $PhSiH_3$.

Product (3,4-dihydroquinoline-1(2*H*)-carbaldehyde). ^{1}H-NMR ($CDCl_3$, 400 MHz)□ major isomer δ 8.76 (s, 1H), 7.24 – 7.04 (m, 4H), 3.81 – 3.78 (m, 2H), 2.80 (t, J = 6.4 Hz, 2H), 1.97 – 1.91 (m, 2H); minor isomer δ 8.30 (s, 0.09H), 7.42 – 7.30 (m, 0.36H), 3.64 – 3.62 (m,0.18H), 2.89 (t, J = 6.7 Hz, 0.18H), 2.05 – 1.99 (m, 0.18H).

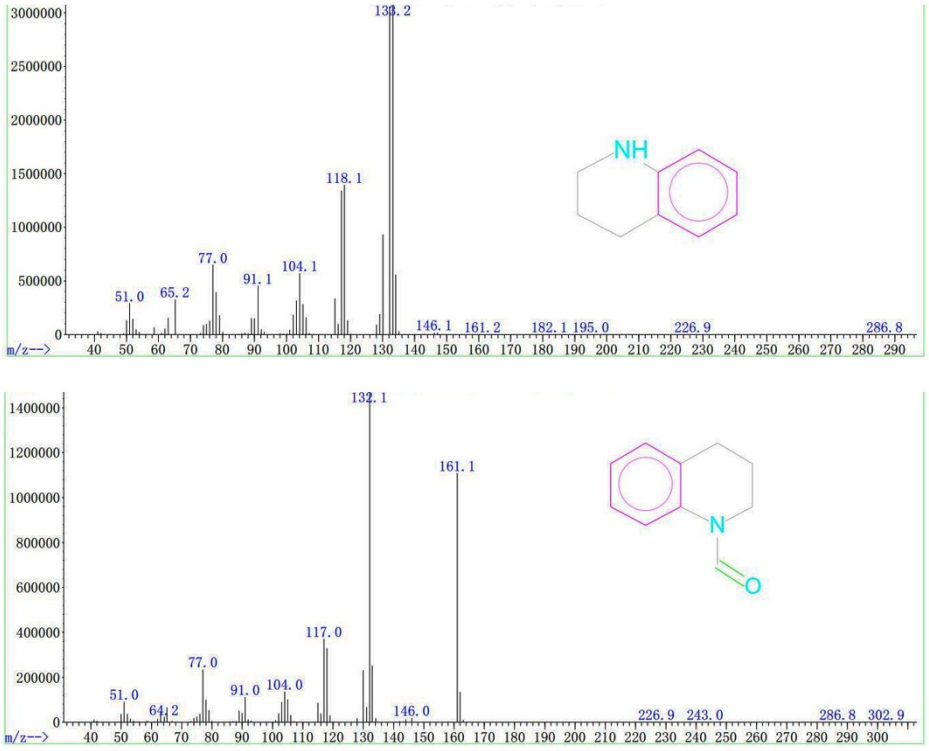

Figure S21. 1,2,3,4-tetrahydroquinoline and 3,4-dihydroquinoline-1(2*H*)-carbaldehyde.

Table S2. Summary of high performance metal-based catalysts for *N*-formylation.

Catalyst	Metal	Hydrosilane	Reaction Conditions			Yield (%)	Reference
			T (°C)	P_{CO2} (MPa)	Time (h)		
PdNPore	Pd	$PhSiH_3$	60	1	20	90	*Asian J. Org. Chem.* 2022, e202200064
Zn powder	Zn	$(EtO)_3SiH$	120	1.5	24	80	*Chin. J. Chem.* 2020, 38, 1057-1064
Br-PMOF(Ir)	Ir	$PhSiH_3$	25	0.1	43	83	*Chem. Eur. J.* 2022, e202200555
Pd@HMP-1	Pd	diphenylmethylsilane	60	1	20	93	*ChemCatChem* 2017, 9, 1939-1946
Pd-PS-amtp	Pd	poly(methyl-hydrosiloxane)	50	1	10	96	*ChemistrySelect* 2019, 4, 3961-3972
ZnO+TBAB	Zn	$PhSiH_3$	40	1	2	98	*Catal. Commun.* 2021, 149, 106195
$Pt_1/Ti_{3-x}C_2T_y$	Pt	Et_3SiH	140	1	10	97	*J. Am. Chem. Soc.* 2019, 141, 4086-4093
Zn-TpPa	Zn	$PhSiH_3$	30	0.1	12	97.5	*Appl. Catal B-Environ.* 2021, 294, 120238
$Zn(OAc)_2$@P(BiPy-DVB)-1	Zn	$PhSiH_3$	30	0.1	5	94	*J. CO_2 Util.* 2022, 65, 102214
ZnPc/g-C_3N_4	Zn	$PhSiH_3$	20 W LED	0.1	24	95	*Catal. Sci. Technol.* 2022, 12, 2688-2702
$Cu/BiVO_4$	Cu	$PhSiH_3$	20 W LED	0.1	24	64	*J. CO_2 Util.* 2021, 45, 101402
Ni-SAs/NPs@BNCNTs	**Ni**	**$PhSiH_3$**	**0.2 W/cm²**	**0.1**	**12**	**95**	**This work**